Journal of Computational Physics 229 (2010) 145–167

Contents lists available at ScienceDirect

Journal of Computational Physics

journal homepage: www.elsevier.com/locate/jcp

Finite element form of FDV for widely varying flowfields

G.A. Richardson [a,b,*], J.T. Cassibry [a,c], T.J. Chung [a], S.T. Wu [b]

[a] Department of Mechanical and Aerospace Engineering, University of Alabama in Huntsville, Huntsville, AL 35899, United States
[b] Center for Space Plasma and Aeronomic Research, University of Alabama in Huntsville, Huntsville, AL 35899, United States
[c] Propulsion Research Center, University of Alabama in Huntsville, Huntsville, AL 35899, United States

ARTICLE INFO

Article history:
Received 21 October 2008
Received in revised form 18 September 2009
Accepted 21 September 2009
Available online 27 September 2009

Keywords:
Hydrodynamics
Numerical methods
Finite element
Shock waves
Special relativity

ABSTRACT

We present the Flowfield Dependent Variation (FDV) method for physical applications that have widely varying spatial and temporal scales. Our motivation is to develop a versatile numerical method that is accurate and stable in simulations with complex geometries and with wide variations in space and time scales. The use of a finite element formulation adds capabilities such as flexible grid geometries and exact enforcement of Neumann boundary conditions. While finite element schemes are used extensively by researchers solving computational fluid dynamics in many engineering fields, their use in space physics, astrophysical fluids and laboratory magnetohydrodynamic simulations with shocks has been predominantly overlooked. The FDV method is unique in that numerical diffusion is derived from physical parameters rather than traditional artificial viscosity methods. Numerical instabilities account for most of the difficulties when capturing shocks in these regimes. The first part of this paper concentrates on the presentation of our numerical method formulation for Newtonian and relativistic hydrodynamics. In the second part we present several standard simulation examples that test the method's limitations and verify the FDV method. We show that our finite element formulation is stable and accurate for a range of both Mach numbers and Lorentz factors in one-dimensional test problems. We also present the converging/diverging nozzle which contains both incompressible and compressible flow in the flowfield over a range of subsonic and supersonic regions. We demonstrate the stability of our method and the accuracy by comparison with the results of other methods including the finite difference Total Variation Diminishing method. We explore the use of FDV for both non-relativistic and relativistic fluids (hydrodynamics) with strong shocks in order to establish the effectiveness in future applications of this method in astrophysical and laboratory plasma environments.

1. Introduction

Many research fields have become strongly dependent on computational simulations to study unobservable physical processes. In these cases, computational approaches are more practical and economical. The theoretical modeling of the complex physical processes are guided and verified by numerical simulations. Finite difference schemes and finite volume (based on finite difference) schemes are the most common numerical schemes in the astrophysical and plasma physics literature. A very thorough review of methods used in relativistic flows can be found in [14,23]. The literature shows a wide variety of numerical schemes with one obvious exception, the use of finite element schemes [24,29]. This is likely due to the compu-

* Corresponding author. Address: Department of Mechanical and Aerospace Engineering, University of Alabama in Huntsville, 301 Sparkman Drive, TH N269, Huntsville, AL 35899, United States.
E-mail address: georgia.richardson@uah.edu (G.A. Richardson).

0021-9991/$ - see front matter © 2009 Elsevier Inc. All rights reserved.
doi:10.1016/j.jcp.2009.09.023

tational restrictions on finite element schemes that have only recently been overcome. There are a number of finite difference based schemes which have been utilized for laboratory scale magnetohydrodynamic (MHD) modeling. For example, MACH2, an axisymmetric 2D non-ideal MHD code, uses a finite volume via finite difference scheme with a second order van Leer method to compute the fluxes for convection [22,26]. Sankaran et al. [32] developed a flux-limited approach with characteristics-splitting techniques to satisfy the Rankine–Hugoniot relations. Several codes are based on the MUSCL-type limited reconstruction principle [3,15,27,38,39]. Comparatively, there has been little work involving finite element schemes in which both the physical and logical mesh are permitted to be unstructured. NIMROD is among the most widely used codes within the fusion community to study magnetically confined plasmas, and has a finite element discretization [16,36,37]. However, it does not have a shock solver.

The Flowfield Dependent Variation (FDV) method was first introduced for engineering applications where incompressible and compressible flow regions exist in the same flowfield [8,9,33,43]. The method was further developed for non-ideal relativistic hydrodynamic flows using a finite element approach [28,29]. The concept was to have a single method accurately solve the entire flowfield even when multiple regions contained flows as different as compressible versus incompressible or laminar versus turbulent. The FDV method uses physical flow parameters (such as the Mach number, Reynolds number, Lorentz number, etc.) to identify the type of flow and the best solution method for that type of flow. The method reduces to previously established numerical schemes if specific indicators are set to constant values. In other words, the FDV method was developed as a way to incorporate multiple solution methods into a single computational domain, while automatically recognizing which method is needed in each area of the flowfield. Most other methods are developed for specific applications and are highly accurate for their purpose, but are not able to solve a range of applications. The FDV method is designed to accurately solve a wider variety and wider scale of problems.

Current numerical schemes used in astrophysics and laboratory plasma, based on finite difference and finite volume schemes, have proven to be reliable [4,5,10,13,18]. However, finite difference methods still have some inherent limitations due to the finite difference formulation. Difficulties still exist in the modeling of phenomena with inherent spatial and temporal scale differences such as discontinuities. For example, in the flow region where a shock wave is traveling, the physical properties of the flow are rapidly changing. In the region the shock has already interacted, the changes are on a much smaller time scale. A highly diffusive solution will result if a large amount of damping is forced in both regions. With FDV, the method will identify the shock so that only limited sections of the flow will be damped. With a finite element scheme, complex geometries (non-structured grids), exact enforcement of Neumann boundary conditions, and four-dimensional adaptive mesh (time and space) can also be applied. The importance of examining finite element schemes for astrophysical problems is becoming evident with the desire to model problems with diverse spacial and temporal scale variations such as relativistic jet formation and propagation and gamma-ray burst studies. Finite element techniques have become the standard in fields such as aerospace engineering, and these techniques have been proven stable and reliable in a wide range of environments [9,44]. In general, finite element schemes are mathematically more rigorous than other schemes, and in the past this has meant they were computationally more expensive and not practical for shock capturing in laboratory MHD and astrophysical applications which are already computationally complex in nature. Mathematical research has lead to new methods for handling the large matrix inversions necessary, making finite element schemes a realistic option for most fluid simulations [31].

In this paper we explore the stability and accuracy of the FDV method in finite element form for use in both non-relativistic and relativistic phenomena where strong shocks are present. In Section 2 we discuss the conservation form of the governing equations. The formulation of these equations can affect the accuracy and efficiency of the numerical method. Section 3 contains a description of the FDV method and the use of finite element formulation for our numerical scheme. We also discuss the use of GMRES for the matrix inversion and the time step constraints. The verification of the finite element FDV method is presented in Section 4. The computational community has adopted a set of "standard" test problems for hydrodynamic shocks. Included in this study are three non-relativistic and two relativistic shock test problems. Additionally, a smooth sine wave and advection test (both with periodic boundaries) and a converging/diverging (de Laval) nozzle to demonstrate the FDV method for flowfields with regions of both incompressible and compressible flow have been included. The first non-relativistic shock case is a simple traveling square wave. The second is the shock heating problem of Noh [25]. The third is Sod's shock tube [35] solved for a variety of Mach numbers. The first of the special relativistic test problems used in this paper is the standard mildly relativistic shock tube problem introduced by Centrilla and Wilson [7] and Hawley et al. [17]. The second problem set that will be addressed is the relativistic shock heating problem [6]. The shock heating problem is popular because it simulates strongly relativistic shocks with very high Lorentz factors. The technique described in this paper is the first finite element scheme to be applied to these relativistic flow problems. Finally, the de Laval converging/diverging nozzle is solved with regions of both incompressible and compressible flow. A summary of our results and the advantages of FDV are given in Section 5. The purpose of this paper is to verify our numerical technique over widely varying flowfields, specifically those found in both laboratory and stellar magnetic reconnection problems.

2. Governing hydrodynamic equations in conservation form

The governing hydrodynamic equations can be derived in several different forms. In order to ensure the constraints of the conservation laws, the hydrodynamic equations are solved in this study in terms of their conservation variables rather than

their primitive variables (pressure, velocity, density, etc.). Conservation variables are found from writing the governing physical equations in conservation form (mass, energy and momentum) as will be demonstrated below. After the computations are complete, the conservation variables can be reduced back to the primitive variables. To allow relativistic problems to be considered, a four-dimensional spacetime (Time + 3D Space) approach is made. This approach leads to the use of a four-velocity which is related to the three-velocity by $U^\alpha = (W, u^1, u^2, u^3)$ where W is the Lorentz factor (the relativistic representation of velocity) defined by $W = (1 - u_i u^i)^{-1/2}$ and u^i is the three-velocity defined by $u^i = \frac{\partial x^i}{\partial t}$. Eq. (1) shows the format for a system of ideal three-dimensional relativistic hydrodynamic equations in conservation form and general coordinates. The equations are solve with natural units (the speed of light c and the gravitational constant G are equal to 1). The index i labels the physical dimension, $\mathbf{U}$ contains the conservation variables, $\mathbf{F^i}$ the convection (advection) terms, and $\mathbf{S}$ the source terms. Here we include the source terms to facilitate the geometry of the converging/diverging nozzle problem and non-ideal and general relativistic problems. The source term is not present in all cases.

$$\frac{\partial \mathbf{U}}{\partial t} + \frac{\partial \mathbf{F^i}}{\partial x_i} = \mathbf{S}. \tag{1}$$

Standard tensor notation is used in these equations. Four-dimensional spacetime parameters are written with Greek indices (eg. $T^{\mu\upsilon}$), while three-dimensional space parameters have Latin indices (eg. $\frac{\partial \mathbf{F^i}}{\partial x_i}$). The three-dimensional conservation equations are derived from the conservation of mass density J^α and the conservation of the stress energy tensor $T^{\alpha\beta}$,

$$\nabla_\mu J^\mu = 0, \tag{2}$$

$$\nabla_\mu T^{\mu\upsilon} = T^{\mu\upsilon}_{;\mu} = T^{\mu\upsilon}_{,\mu} + T^{\alpha\upsilon}\Gamma^\mu_{\alpha\mu} + T^{\mu\alpha}\Gamma^\upsilon_{\alpha\mu} = 0. \tag{3}$$

Note that ";" is the tensor notation for the expansion in Eq. (3) and "," is the tensor notation for the partial derivative $U_{,i} = \frac{\partial U}{\partial x^i}$. As will be shown below, the last two terms on the right of Eq. (3) only appear for curvilinear metrics. The ideal form of the stress energy tensor which excludes viscosity and heat flux is,

$$T^{\mu\upsilon} = \rho h u^\mu u^\upsilon + P g^{\mu\upsilon}. \tag{4}$$

The tensor reveals both energy and momentum conservation. For example, T^{00} is the 0 component of the four momentum across the surface of constant time. The 0 component of the four momentum is energy, so T^{00} is equal to the energy density. The flux of energy across a constant spatial surface is T^{0j}. T^{i0} is the flux of momentum across the surface of constant time, the i momentum density. T^{ij} is the flux of momentum across a constant spatial surface. The metric terms, $g^{\alpha\beta}$, define the environment and are an important component for problems solved in curvilinear space. The metric defines the physical time and space correlation and any curvature. For example, the spacetime around a black hole is curved in comparison with the flat spacetime found in Newtonian physics. The Kerr metric is commonly used for simulations around a black hole and the line element for a non-spinning black hole of mass M is given by $ds^2 = -\left(\frac{r-2M}{r}\right)dt^2 + r^2 sin^2\theta\, d\phi^2 + \left(\frac{r}{r-2M}\right)dr^2 + r^2\, d\theta^2$. In this example, the source terms are calculated by the Christoffel symbols,

$$\Gamma^\alpha_{\beta\gamma} = g^{\alpha\mu}\Gamma_{\mu\beta\gamma} = \frac{1}{2}g^{\alpha\mu}(g_{\mu\beta,\gamma} + g_{\mu\gamma,\beta} - g_{\beta\gamma,\mu}). \tag{5}$$

In special relativity, the Minkowski line element, $ds^2 = -dt^2 + dx^2 + dy^2 + dz^2$, is used to determine the metric. No source terms result from the metric in special relativity, but there may be source terms due to physical components such as magnetic fields. An enjoyable and understandable discussion of relativity, metrics and tensor notation can be found in Schutz [34].

Eq. (6) contains the conservation variables. In this equation, the first row corresponds to the conservation of mass, the next three for the three-dimensional conservation of momentum and the final row for the conservation of energy. The primitive variables in this example include ρ, u^i, P, and h corresponding to the density, three-velocity, pressure and mass equivalent (specific) enthalpy, respectively. Additionally, g is defined as the determinate of the metric.

$$\mathbf{U} = \sqrt{-g}\begin{bmatrix} \rho W \\ (\rho h W u^1 + P g^{01}) \\ (\rho h W u^2 + P g^{02}) \\ (\rho h W u^3 + P g^{03}) \\ (\rho h W W + P g^{00}) \end{bmatrix}. \tag{6}$$

The convection (advection) terms, $\mathbf{F^i}$ are,

$$\mathbf{F}^i = \sqrt{-g}\begin{bmatrix} \rho u^i \\ (\rho h u^i u^1 + P g^{11}\delta^i_1) \\ (\rho h u^i u^2 + P g^{22}\delta^i_2) \\ (\rho h u^i u^3 + P g^{33}\delta^i_3) \\ (\rho h W u^i + P g^{i0}) \end{bmatrix}, \tag{7}$$

and the source terms, **S** are,

$$\mathbf{S} = \sqrt{-g}\begin{bmatrix} 0 \\ T^{\mu\alpha}\Gamma^1_{\alpha\mu} \\ T^{\mu\alpha}\Gamma^2_{\alpha\mu} \\ T^{\mu\alpha}\Gamma^3_{\alpha\mu} \\ T^{\mu\alpha}\Gamma^0_{\alpha\mu} \end{bmatrix}. \tag{8}$$

Eqs. (6)–(8) are used in the special relativistic test problems presented in Section 4. In these equations, pressure is related to the other variables by the equation of state, $P = P(\rho, \varepsilon)$ and is regulated by the Kronecker delta, δ_{ij}. For an ideal gas, the equation of state is given by, $P = \rho\varepsilon(\gamma - 1)$, where γ is the ideal gas adiabatic exponent and ε is the specific internal energy. The specific enthalpy is defined $h = 1 + \varepsilon + \frac{P}{\rho}$ which includes the relativistic rest mass energy term ($E = mc^2$). Once the conservation equations have been solved, the primitive variables are recovered from the conservation variables shown in Eq. (6). The detailed derivation of the above equations in a general relativistic environment can be found in Richardson and Chung [29].

In order to resolve the primitive variables (u_1, u_2, u_3, p, ρ) from the conservation variables $(U_1, U_2, U_3, U_4, U_5)$ several methods were compared. The most common methods for solving the fourth order equation that results in the one-dimensional hydrodynamic case are iterative methods such as a Newton–Rhapson method. A disadvantage to using an iterative method is found in the case of a high Lorentz shock. Iteration methods require a starting point value for the Lorentz factor and since that value can range from one to over a thousand, estimating an initial guess can be difficult. Other methods have been developed that exactly solve the fourth order equation by the method of radicals [28]. In this case, four solutions result and the simulation code must be able to determine which is the correct solution. For our simulations there is always only one positive solution. For more complex equation systems like those in MHD, a higher order equation results which can not be solved using radicals and numerical approximations must be utilized. Our choice of solutions is to compute the eigenvalues from the matrix formed using the polynomial coefficients. Since the number of solutions will always equal the order of the polynomial, the correct physical solution must still be determined. Another iterative approach which is less complex can be found in Del Zanna et al. [12]. In this method, an estimate of the velocity is necessary, but the high Lorentz value problem is avoided since the velocity value will always be between 0 and 1.

Since both relativistic and non-relativistic test problems are used to validate FDV, the non-relativistic form is included for completeness. The non-relativistic form can be found using the three-velocity instead of the four-velocity. The removal of the Lorentz factor simplifies the equations greatly since the primitive to conservation conversion no longer has a higher-order equation to be solved. Additionally, the energy term is simplified since the rest mass energy term is no longer a factor and the gravitational source terms are removed. The non-relativistic ideal conservation equations are;

$$\mathbf{U} = \begin{bmatrix} \rho \\ \rho v^1 \\ \rho v^2 \\ \rho v^3 \\ E \end{bmatrix}, \quad \mathbf{F}^i = \begin{bmatrix} \rho v^i \\ \rho v^i v^1 + P\delta^i_1 \\ \rho v^i v^2 + P\delta^i_2 \\ \rho v^i v^3 + P\delta^i_3 \\ v^i E + v^i P \end{bmatrix}. \tag{9}$$

The quasi one-dimensional equations used in the converging/diverging nozzle are also included.

$$\mathbf{U} = \begin{bmatrix} \rho A \\ \rho v^1 A \\ EA \end{bmatrix}, \quad \mathbf{F}^1 = \begin{bmatrix} \rho v^i A \\ (\rho v^1 v^1 + P)A \\ (v^1 E + v^1 P)A \end{bmatrix}, \quad \mathbf{S} = \begin{bmatrix} 0 \\ P\frac{\partial A}{\partial x^1} \\ 0 \end{bmatrix}. \tag{10}$$

Energy is give by the relationship $P = (\gamma - 1)\left[E - \frac{1}{2}\rho v^2\right]$ where P is the pressure, v^i the three-velocity, E the total energy, A the cross sectional area perpendicular to the flow and γ the specific heat ratio.

3. Flowfield Dependent Variation method

3.1. FDV formulation

The equations to be solved numerically in most space and laboratory plasmas and in astrophysical simulations, including the relativistic hydrodynamic equations in Section 2, are non-linear partial differential equations (PDEs). Common forms of PDEs include hyperbolic, elliptical and parabolic. The equations found in many of these scenarios are of a mixed form referring to a combination of one or more of the common types. The physical diffusion terms are indicated by the elliptical nature of the PDEs. When these diffusion terms and/or widely disparate source terms (gravity, magnetic fields, etc.) are added to the governing equations, the complexity of the equations noticeably increases. In many cases, the complexity of the physics outweighs the attention given to the numerical treatments. In some cases the dominating nature of the flow will vary across the simulation domain. In these cases it is desirable that the simulation method recognize the different regions and automati-

cally dictate the appropriate numerical scheme. Otherwise, a predetermined numerical scheme will influence the solution. In many existing schemes, the numerical viscosities are calculated from the local flowfield velocities, suggesting that they are indeed flowfield dependent. These may be adequate if the flow is dominated by convection only. If the flow is dominated not only by convection but by other physical aspects such as gravity, electromagnetic forces, turbulence, or radiation, then special treatments may be necessary. For these reasons, the FDV method has been examined.

In the FDV formulation the conservation equations are first expanded using a special form of the Taylor series where n denotes the time index. This expansion is done with the addition of the first and second order flowfield-dependent variation parameters, s_a and s_b.

$$\mathbf{U}^{n+1} = \mathbf{U}^n + \Delta t \frac{\partial \mathbf{U}^{n+s_a}}{\partial t} + \frac{\Delta t^2}{2} \frac{\partial^2 \mathbf{U}^{n+s_b}}{\partial t^2} + O(\Delta t^3), \tag{11}$$

$$\frac{\partial \mathbf{U}^{n+s_a}}{\partial t} = \frac{\partial \mathbf{U}^n}{\partial t} + s_a \frac{\partial \Delta \mathbf{U}^{n+1}}{\partial t} \quad 0 < s_a \leqslant 1, \tag{12}$$

$$\frac{\partial^2 \mathbf{U}^{n+s_b}}{\partial t^2} = \frac{\partial^2 \mathbf{U}^n}{\partial t^2} + s_b \frac{\partial^2 \Delta \mathbf{U}^{n+1}}{\partial t^2} \quad 0 < s_b \leqslant 1. \tag{13}$$

With,

$$\Delta U^{n+1} = U^{n+1} - U^n, \tag{14}$$

and

$$\Delta U^{n+1} = \Delta t \left(\frac{\partial U^n}{\partial t} + s_a \frac{\partial \Delta U^{n+1}}{\partial t} \right) + \frac{\Delta t^2}{2} \left(\frac{\partial^2 U^n}{\partial t^2} + s_b \frac{\partial^2 \Delta U^{n+1}}{\partial t^2} \right) + o(\Delta t^3). \tag{15}$$

3.2. FDV parameters

The FDV method is unique in that the FDV parameters act as weight functions between an implicit and explicit method. This can be seen from Eq. (15). If the FDV parameters s_a and s_b are set to zero the method is explicit. If s_a and s_b are set to one the method is implicit. Since the parameters are calculated between zero and one, the method is weighted more towards one or the other. The FDV parameters are calculated from physical changes in the flow, which are reflected in such dimensionless parameters as the Mach number or Lorentz factor. The appropriate dimensionless parameter is determined by the equations being solved. For example in viscous flows, the non-dimensional form of the hydrodynamic equations includes the Reynolds number and Prandtl number. In the ideal form, the equations have either the Mach number or Lorentz factor for the dimensionless velocity. More complex MHD flows will have the velocity normalized with the Alfvén wave speed and magnetic Reynolds number. The FDV parameters are calculated between every adjacent spatial node and at each numerical time interval providing physical information about changes in the flow. If shocks are detected, the method adapts to an explicit form, while a smooth flow is better solved with an implicit form. This physical information dictates the amount of numerical diffusion necessary. For example, if the Mach number remains constant in space and time, the appropriate FDV parameter also remains fixed. If the difference in Mach number between adjacent nodal points is non-zero, the parameter adjusts. The amount of adjustment depends on the magnitude of the Mach number change between two spatial nodes. The resulting governing equations are capable of resolving widely disparate length and time scales.

In order to widen the physical interpretation of the FDV parameters, s_a is separated into a convection parameter s_1 and source term parameter s_5. The source term parameters are relevant for our nozzle simulation and for metrics with non-canceling Christoffel symbols like the Kerr metric. Similar arguments apply to the second order FDV parameter s_b leading to s_2 for convection and s_6 for the source term. The parameters s_3 and s_4 are reserved for non-ideal simulations with diffusion terms (ie. [29]). The second order FDV parameters are chosen to be exponentially proportional to the first order FDV parameters. This choice is made to ensure a connection between the first order FDV parameters which tend to assure accuracy of the solution, and the second order FDV parameters which provide numerical stability (diffusion).

In the following modified FDV equations defining the first order term, "I" is the indicator being used. For our non-relativistic simulations the Mach number is calculated. In the relativistic cases, the Lorentz number is used. It is important to note that the minimum physical Lorentz number is one while the Mach number can be zero. The maximum and minimum indicator values are determined from the set of nodes that make up each element and denoted by $I_{\max}$ and $I_{\min}$. The FDV parameters are calculated for each element at each timestep.

$$s_a = \begin{cases} \min(r, 1) & r > \alpha \\ \alpha & r < \alpha, I_{\min} \neq I_{global} \\ 1 & I_{\min} = I_{global} \end{cases} \tag{16}$$

$$r = \frac{\sqrt{I_{\max}^2 - I_{\min}^2}}{I_{\min}} \tag{17}$$

The s_a parameter will always fall between α and 1, $(\alpha < s_a \leqslant 1)$ where $0 < \alpha < 1$. In the above equation, $I_{global} = 0$ if the Mach number is used or $I_{global} = 1$ if the Lorentz factor is used. The second order convection parameter s_b is defined;

$$s_b = s_a^{\eta}, 0 \leqslant \eta \leqslant 1. \tag{18}$$

The second order parameter is constrained by $\alpha^{\eta} < s_b \leqslant 1$. In the above equations, α and η are user defined variables that depend on the problem being solved. As will be seen in Section 4 the values for α and η vary depending on the smooth or discontinuous nature of the test problem. The 1D non-relativistic shock tube example is used to demonstrate the FDV parameters. Initially two regions of an ideal gas are separated by a wall. The two regions are at different pressures. When the wall is removed, the high pressure gas quickly flows into the lower pressure region. With the correct initial conditions, a shock forms in the simulation. Fig. 1 shows how the FDV parameter s_1 varies as the Mach number in the flowfield varies. The initial conditions for this problem have the removable wall at $x = 0$ and the high pressure gas on the left side of the computational domain. The FDV defined variable settings include $\alpha = 0.25$ and $\eta = 0.01$ from Eqs. (16) and (18). The results show that the numerical method (i.e. the FDV parameter) recognizes areas of physical flow changes. The Mach number is changing rapidly in the shocked regions but is not changing in the non-shocked regions. The FDV parameter reflects this in its profile.

The FDV parameters add flexibility to the numerical formulation. When varied, the two parameters assist in the accuracy and stability of the solution. This is demonstrated in Fig. 2 which shows the velocity shock for a 1D shock tube problem. The computational problem is identical in each of the figure cases (i.e. time step, GMRES parameters, initial and boundary conditions), only the variables used to calculate the FDV parameters are changed. In first case, $\alpha = 0.25$ and $\eta = 0.99$, the large value of η causes numerical instabilities to develop. In the second case, $\alpha = 0.25$ and $\eta = 0.01$, the instabilities have been damped with the lower η value. In third case, $\alpha = 0.9$ and $\eta = 0.01$, the α value has been increased causing a less accurate and more diffusive solution. Recall that when the FDV parameters s_a and s_b are near zero the method is explicit and when near one the method is implicit. In case three the solution is weighted to much towards an implicit method and the results are overly damped. The other two cases are not weighted towards either extreme since the s_a parameter can vary between 0.25 and 1 in both.

Other schemes such as the MUSCL-based total variation diminishing algorithm given by Tóth and Odstril [41] use limiters to handle discontinuities and convection. Some limiters are designed to be diffusive in order to better handle discontinuities. Other limiters are dispersive in nature to handle convection. The FDV method can handle these variations within a single formulation. The FDV method has been modified from its original form with the modification of the variation parameters s_a and s_b. The modification assists in maintaining the second order time accuracy of the method and adding stability to flows with stronger shocks.

3.3. Finite element formulation

For our formulations we use a weighted residual method. The resulting residual form of the FDV equations is,

$$\mathbf{R} = \mathbf{A}\Delta\mathbf{U}^{n+1} + \mathbf{E}_i^n \frac{\partial}{\partial x_i}(\Delta\mathbf{U}^{n+1}) + \mathbf{E}_{ij}^n \frac{\partial^2}{\partial x_i \partial x_j}(\Delta\mathbf{U}^{n+1}) - \mathbf{Q}_i^n = 0, \tag{19}$$

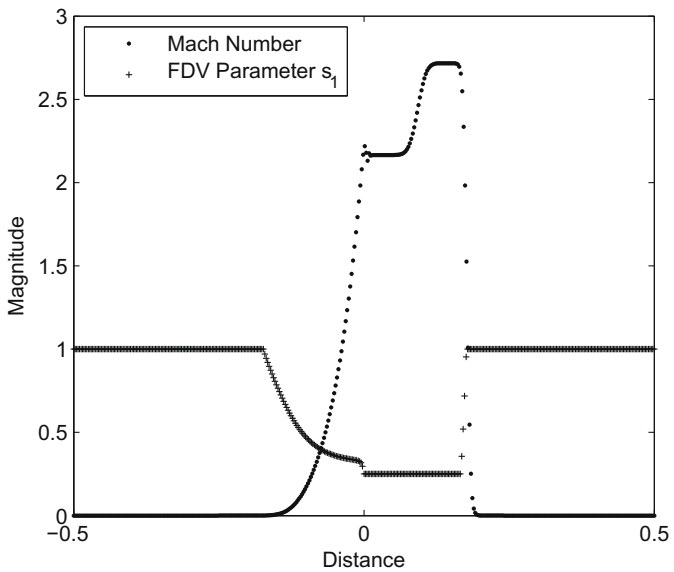

Fig. 1. Mach number and FDV parameter s_1 for the non-relativistic shocktube test problem. The FDV defined variables $\alpha = 0.25$ and $\eta = 0.01$ are defined in Eqs. (16) and (18). This figure shows the relationship between the physical flow parameters and the numerical FDV parameters. Note that the s_1 parameter is minimum with the α parameter.

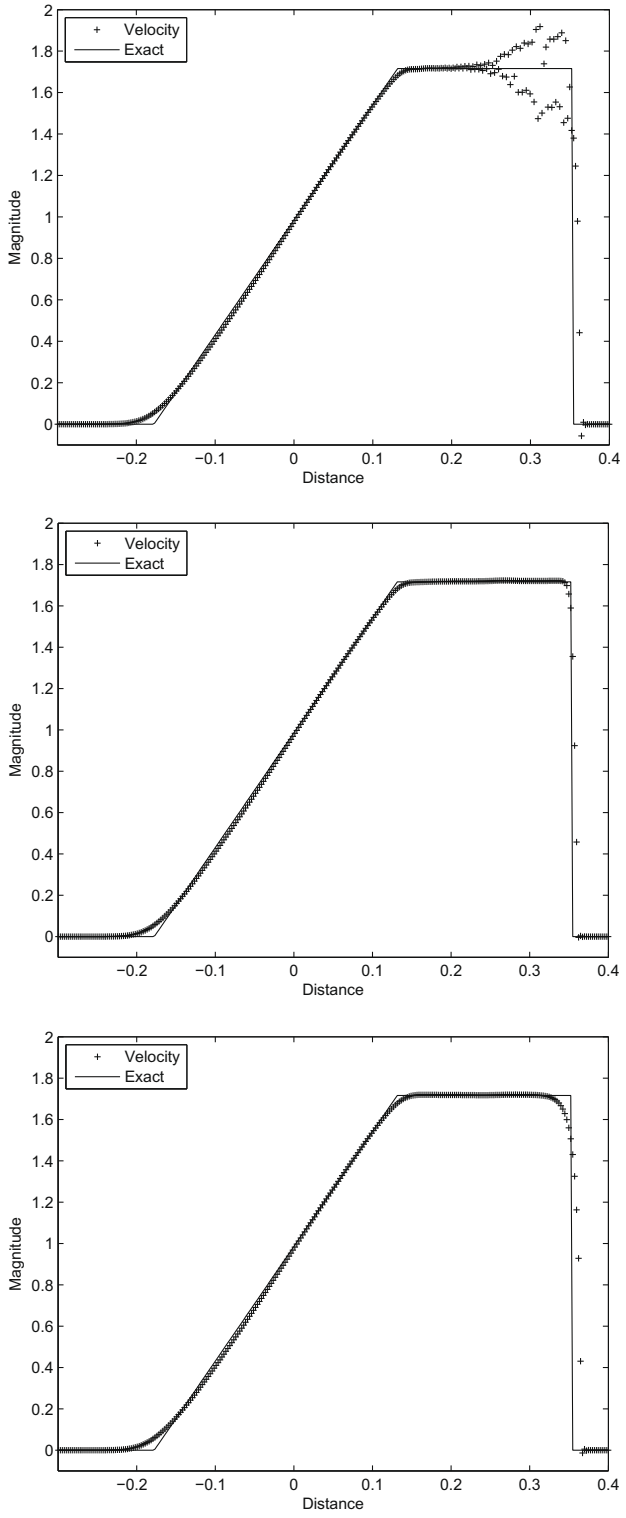

Fig. 2. Velocity shock for the non-relativistic shocktube test problem. The only modifications between the three solutions are the variables used to calculate the FDV parameters. The FDV variables α and η are defined in Eqs. (16) and (18). In the first plot $\alpha = 0.25$ and $\eta = 0.99$, the second $\alpha = 0.25$ and $\eta = 0.01$ and the third $\alpha = 0.9$ and $\eta = 0.01$. A wide difference is seen between the choices in both accuracy and stability.

where $\mathbf{A}, \mathbf{E}_i^n$, and $\mathbf{E}_{ij}^n$ and $\mathbf{Q}_i^n$ contain the information from the convective, diffusion, and source terms. For the cases used in our verification examples these equations reduce to,

$$\mathbf{A} = \mathbf{I} - \Delta t s_5 \mathbf{d} - \frac{\Delta t^2}{2} s_6 \mathbf{d}^2, \tag{20}$$

$$\mathbf{E}_i = \left[\Delta t s_1 \mathbf{a}_i + \frac{\Delta t^2}{2} (s_6 \mathbf{d}\mathbf{a}_i + s_2 \mathbf{d}\mathbf{a}_i) \right]^n, \tag{21}$$

$$\mathbf{E}_{ij} = -s_2 \frac{\Delta t^2}{2} (\mathbf{a}_i \mathbf{a}_j)^n, \text{ and} \tag{22}$$

$$\mathbf{Q}^n = -\frac{\partial}{\partial x_i} \left[\left(\Delta t + \frac{\Delta t^2}{2} \mathbf{d} \right) \mathbf{F}_i^n + \left(\frac{\Delta t^2}{2} \mathbf{a}_i \right) \mathbf{S}^n \right] + \frac{\Delta t^2}{2} \left[\mathbf{a}_i^n \frac{\partial}{\partial x_i} \left(\frac{\partial \mathbf{F}_i^n}{\partial x_i} \right) \right] + \left(\Delta t + \frac{\Delta t^2}{2} \mathbf{d} \right) \mathbf{S}^n. \tag{23}$$

The spacial indices are given by i and j, and n is the time index. The Jacobians for the convection terms are given by $a_i = \frac{\partial F_i}{\partial U}$ and for the source terms by $d = \frac{\partial S}{\partial U}$. These equations represent the modified differential equations as a result of an application of the FDV theory to Eq. (1). Note that, although E_i and E_{ij} are functions of the spatial coordinates, they are considered constants during the time integration steps, and are updated in the next time step. They are placed outside of the differential operators allowing any existing numerical scheme such as finite difference, finite element, or finite volume to be used to discretize Eq. (19). Up to this point in the equation formulation no numerical scheme has been specified. It is at this point that a finite difference, finite volume or finite element scheme is chosen. For the reasons described in Section 1, which included the freedom of non-structured grids and mathematically enforced boundary conditions, we choose a finite element formulation.

The finite element formulation consists of constructing an inner product projecting the residual R of the differential equations, onto a subspace spanned by test functions Φ_α. If the test function is chosen to be the same as the trial function, Φ_β, which separates the variables,

$$\mathbf{U}(x_k, t) = \Phi_\beta(x_k) U_\beta(t), \tag{24}$$

then such an approximation is known as the standard Galerkin finite element scheme given by

$$(\Phi_\alpha, R(\mathbf{U}, \mathbf{F}_i, \mathbf{G}_i, \mathbf{S})) = \int_\Omega \Phi_\alpha \mathbf{R}(\mathbf{U}, \mathbf{F}_i, \mathbf{G}_i, \mathbf{S}) d\Omega = 0. \tag{25}$$

The trial functions are dependent on the element formulation of the mesh, in this case isoparametric elements are used. Integration of Eq. (25) by parts leads to the global form of the assembled finite element equations, with the Neumann boundary functions. In Eq. (25) and the resulting equations below, $\int_\Omega d\Omega$ represents a volume integral and $\int_\Gamma d\Gamma$ a surface integral.

$$(A_{\alpha\beta}\eta_{rs} + B_{\alpha\beta rs}) \Delta U_{\beta s}^{n+1} = H_{\alpha r}^n + N_{\alpha r}^n, \tag{26}$$

$$A_{\alpha\beta} = \int_\Omega \Phi_\alpha \Phi_\beta d\Omega, \tag{27}$$

$$\eta_{rs} = \delta_{rs} + \Delta t s_5 d_{rs} + \frac{\Delta t^2}{2} s_6 d_{rm} d_{ms}, \tag{28}$$

$$\begin{aligned} B_{\alpha\beta rs} = & \int_\Omega \left[-\left(\Delta t (s_1 a_{irs}) + \frac{\Delta t^2}{2} ((s_2 + s_6) d_{rt} a_{its}) \right) \Phi_{\alpha,i} \Phi_\beta \right] d\Omega \\ & + \int_\Omega \left[\frac{\Delta t^2}{2} s_2 (a_{irt} a_{jts}) \Phi_{\alpha,i} \Phi_{\beta,j} \right] d\Omega + \int_\Gamma \left[\Delta t (s_1 a_{irs}) + \frac{\Delta t^2}{2} ((s_2 + s_6) d_{rt} a_{its}) \overset{*}{\underset{\alpha}{\Phi}} \overset{*}{\underset{\beta}{\Phi}} \right] n_i d\Gamma - \int_\Gamma \left[\frac{\Delta t^2}{2} s_2 (a_{irt} a_{jts}) \overset{*}{\underset{\alpha}{\Phi}} \overset{*}{\underset{\beta,j}{\Phi}} \right] n_i d\Gamma, \end{aligned} \tag{29}$$

$$H_{\alpha r}^n = \int_\Omega \left[\Delta t F_{\beta ir}^n + \frac{\Delta t^2}{2} (d_{rs} F_{\beta is}^n + a_{irs} S_{\beta s}^n) \Phi_{\alpha,i} \Phi_\beta \right] d\Omega - \int_\Omega \left[\frac{\Delta t^2}{2} (a_{irs} F_{\beta js}^n) \Phi_{\alpha,i} \Phi_{\beta,j} \right] d\Omega + \int_\Omega \left[\left(\Delta t S_{\beta r}^n + \frac{\Delta^2}{2} d_{rs} S_{\beta s}^n \right) \Phi_\alpha \Phi_\beta \right] d\Omega, \tag{30}$$

$$N_{\alpha r}^n = \int_\Gamma \left(-\left[\Delta t (F_{\beta ir}^n) + \frac{\Delta t^2}{2} (d_{rs} F_{\beta is}^n + a_{irs} S_{\beta s}^n) \right] \overset{*}{\underset{\alpha}{\Phi}} \overset{*}{\underset{\beta}{\Phi}} \right) n_i d\Gamma + \int_\Gamma \left(\frac{\Delta t^2}{2} a_{irs} F_{\beta js}^n \overset{*}{\underset{\alpha}{\Phi}} \overset{*}{\underset{\beta,j}{\Phi}} \right) n_i d\Gamma. \tag{31}$$

The symbol * implies the Neumann boundary test and trial functions. The numerical integration is done using Gaussian Quadrature. Note that if the FDV parameters are set at $s_1 = 0$ and $s_2 = 1$, the above equations reduce to the Taylor Galerkin finite element scheme. The boundary integrals shown in Eqs. (29) and (31) are solved only when Neumann boundary conditions are specified. Due to the finite element formulation, the Neumann boundary conditions are applied without the common constraints found in finite difference schemes (such as phantom nodes). Dirichlet boundary conditions are applied directly to the boundary nodes. If a finite difference formulation is chosen for FDV, the equations reduce to commonly used finite difference schemes when the FDV parameters are fixed at specified values. These schemes include Beam–Warming, Euler explicit and implicit, Three point implicit, Trapezoidal implicit and Leap frog explicit. A discussion of these formulations can be found in Yoon et al. [43].

3.4. Generalized minimal residual application

The resulting system of equations (matrix inversion) is solved using the generalized minimal residual (GMRES) technique [30,20]. This method is a Krylov subspace projection method that minimized the residual norm. The input parameters allowed for GMRES include the maximum number of inner iterations, maximum number of outer iterations and the minimum residual. Once the residual criteria is met, the iterations stop. Other allowable parameters include an initial guess and preconditioners. For these test problems the initial guess and preconditioning options are not used. The solutions found using GMRES converged quickly and large numbers of iterations were not necessary. The standard GMRES settings for the test problems presented in this paper are a maximum of 10 inner iterations and 2 outer iterations with a minimum residual of 1.0E−6. In order to decrease computation time when large matrix inversions are necessary, the equations are reformulated in an element by element format [31]. In this form, smaller matrix inversions are performed on element groupings and then recombined into their global format. The element matrix inversions are also performed using GMRES.

3.5. Timestep constraints

In explicit methods used to solve shock discontinuities, the timestep constraint requires that the fluid information can not travel over more than one spacial element during a single timestep. Explicit methods are generally more accurate for shock simulations. Since implicit methods include both the current and future timesteps in the solution, they are less restrictive. Implicit methods are generally used when a more diffusive problem is being solved. In equation form the explicit constraint leads to $\Delta t < CFL\frac{\Delta x}{V_{max}}$. To ensure this constraint, the velocity term used is the fluid velocity plus the sound speed $V_{max} = u + a$. This problem was studied originally by Courant et al. [11] with *CFL* being the time step constraint number. The timestep used with each test problem in Section 4 is given with the problem and reported in the form $\Delta t < CFL\frac{\Delta x}{V_{max}}$ for easier comparison with other methods.

4. Test cases for FDV verification

Several standard test cases were evaluated to verify the FDV method. The first is a smooth wave with periodic boundary conditions. The second is the scalar advection test problem. These first two problems are not governed by the hydrodynamic equations in Section 2 but rather simple linear equations given with the problem statement. The next set of problems are non-relativistic shock problems including the square wave, Noh shock and the hydrodynamic shock tube which are found by solving Eq. (9). The special relativistic problems including the shock tube and a shock reflection problem are solutions to Eqs. (6)–(8). The final problem is the converging/diverging nozzle which is solved using Eq. (10). As seen in these test problems solved using FDV, the stronger shocks have a more accurate solution when the method is more explicit in nature. The smooth problems are solved with a more implicit nature.

For each test problem, the L1 and L2 Norm errors were calculated as compared with the analytic solution. The L1 Norm errors are found with

$$E_{L1} = \frac{1}{N}\sum_{i=1}^{N}\left[\frac{|S_e(i) - S_c(i)|}{|S_e(i)|}\right], \tag{32}$$

where S_e is the exact solution and S_c is the computed solution. The L2 Norm errors are found with

$$E_{L2} = \left(\frac{\sum_{i=1}^{N}(S_e(i) - S_c(i))^2}{\sum_{i=1}^{N}(S_e(i))^2}\right)^{\frac{1}{2}}, \text{ and} \tag{33}$$

The maximum errors are found with,

$$E_{L\infty} = \max_{(1,\ldots,N)}\left[\frac{|S_e(i) - S_c(i)|}{|S_e(i)|}\right]. \tag{34}$$

When plotted against the mesh size on a loglog plot, the resulting slope of a best linear fit is related to the convergence rate of the method.

$$\log(|error|) \approx p\log(x) + \log(c). \tag{35}$$

Here p is the order of convergence and c the constant of proportionality.

4.1. Smooth wave test case

The first test case is a smooth sine wave with periodic boundary conditions proposed by Jiang and Shu [19]. In this test case, the FDV method is used to solve the linear equation,

$$u_t + u_x = 0, \quad -1 \leqslant x \leqslant 1. \tag{36}$$

The initial condition is,

$$u(x,0) = \sin(\pi x), \tag{37}$$

with periodic boundary conditions. For this problem the FDV defined variables are $\alpha = 0.9$ and $\eta = 0.5$. The higher α and lower η indicates a more implicit nature of the equations. The FDV parameters are calculated using a normalized velocity for the indicator in Eqs. (16) and (17). The time step is calculated using $\Delta t = 0.3\frac{\Delta x}{V_{max\,wave}}$. Fig. 3 shows the FDV results of this smooth test problem with 50 nodes at $t = 1$ s plotted over the exact wave. The lower two panels of the figure show the L1 and L2 Norm values for 100–1600 nodes plotted on a loglog scale. The slopes of the linear fit of these errors give an indication of the numerical method's convergence rate. The slope values for the L1 and L2 Norms are −0.90 and −0.98, respectively. These results reflect the impact of the s_b parameter to lower the method accuracy to first order in smooth cases.

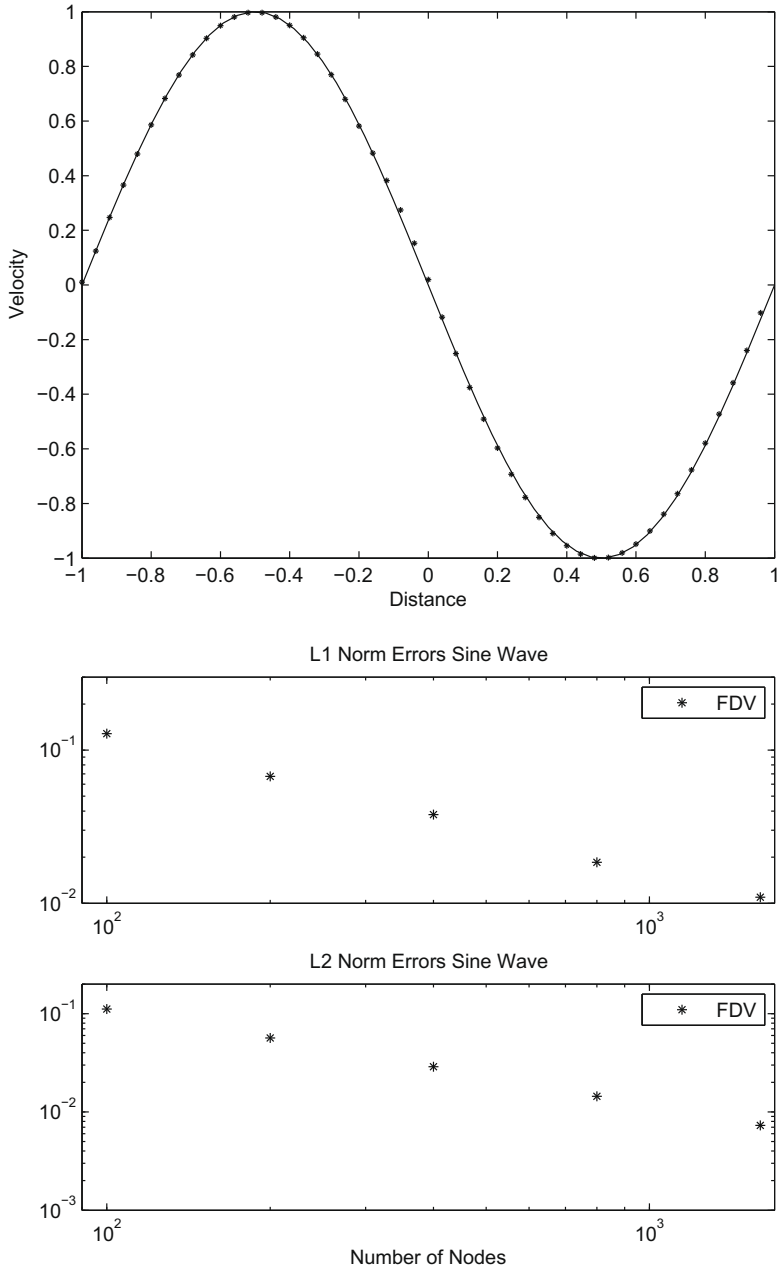

Fig. 3. *Upper Plot:* Smooth sine wave with periodic boundary conditions given in Eqs. (36) and (37). The plot is shown at $t = 1$ s with 50 nodes and $\Delta t = 0.3\frac{\Delta x}{V_{max\,wave}}$. The FDV defined variables are $\alpha = 0.9$ and $\eta = 0.5$. *Lower Plot:* FDV convergence rate for the L1 Norm and L2 Norm density errors of the sine wave using domain grids from 100 to 1600 nodes. The L1 Norm and L2 Norm linear best-fit slopes are −0.90 and −0.98.

4.2. Scalar advection test case

The second test case is the scalar advection test case proposed by Jiang and Shu [19]. This test problem solves the same linear equation as Eq. (36), but with a much more complicated set of initial conditions. The problem has periodic boundary conditions and is stated as follows:

$$u_t + u_x = 0, \quad -1 \leqslant x \leqslant 1, \tag{38}$$

$$u(x,0) = u_o(x), \tag{39}$$

$$\begin{aligned} u_o(x) &= \tfrac{1}{6}[G(x,\beta,z-\delta) + G(x,\beta,z+\delta) + 4G(x,\beta,z)] \\ &\quad \text{when } -0.8 \leqslant x \leqslant -0.6, \\ u_o(x) &= 1 \\ &\quad \text{when } -0.4 \leqslant x \leqslant -0.2, \\ u_o(x) &= 1 - |10(x-0.1)| \\ &\quad \text{when } 0.0 \leqslant x \leqslant 0.2, \\ u_o(x) &= \tfrac{1}{6}[F(x,\lambda,a-\delta) + F(x,\lambda,a+\delta) + 4F(x,\lambda,a)] \\ &\quad \text{when } 0.4 \leqslant x \leqslant 0.6, \\ u_o(x) &= 0 \\ &\quad \text{otherwise}, \end{aligned} \tag{40}$$

$$G(x,\beta,z) = e^{-\beta(x-z)^2}, \tag{41}$$

$$F(x,\lambda,a) = \sqrt{max(1-\lambda^2(x-a)^2, 0)}, \tag{42}$$

with $a = 0.5, z = -0.7, \delta = 0.005, \lambda = 10$ and $\beta = \frac{log2}{36\delta^2}$. Results from this test case are shown in Fig. 4 where 200 nodes were used. The timestep is given by $\Delta t = 0.1\frac{\Delta x}{V_{max\,wave}}$ and the FDV defined variables were set as $\alpha = 0.9$ and $\eta = 0.5$. This results demonstrates the ability of the FDV method with complex flow features and boundary conditions. The geometric waves move to the right and wrap around the left boundary when they reach the right boundary. A total time of $t = 2$ s was used.

4.3. Shock test cases

The initial conditions of the shock cases are summarized in Table 1.

In the non-relativistic cases we ran comparison tests using the finite difference Total Variation Diminishing (TVD) method. The TVD code is based on the MUSCL algorithm by Tóth and Odstril [41]. Specifically, we are using Yee's high order Lax-

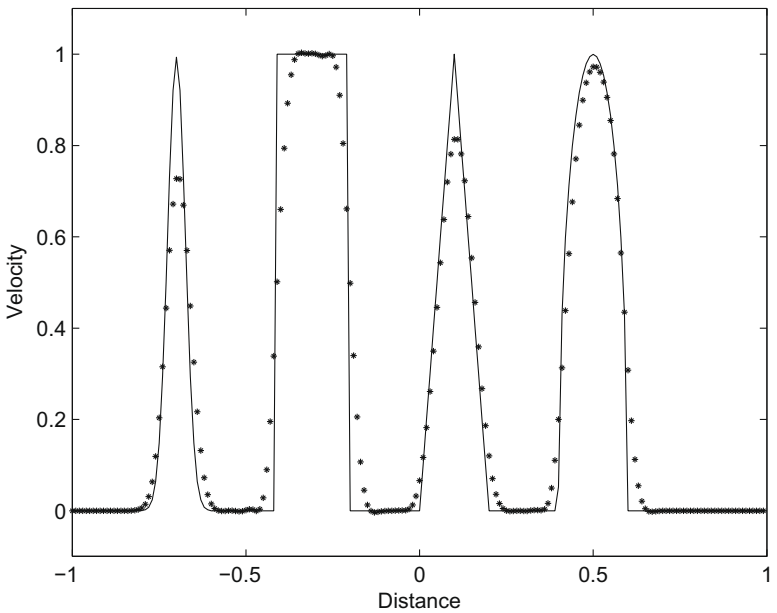

Fig. 4. Scalar advection test case with periodic boundary conditions given by Eqs. (38)–(41). The plot is shown at $t = 2$ s and 200 nodes were used with $\Delta t = 0.1\frac{\Delta x}{V_{max\,wave}}$. The FDV defined variables are $\alpha = 0.9$ and $\eta = 0.5$.

Friedrichs TVD scheme because it does not use a Riemann solver [42]. We chose this method because it can be applied to an arbitrary system of conservation laws without a knowledge of the characteristic waves. For the comparison with FDV we chose the minmod, monotonized central, superbee limiters. The minmod and superbee are the most and least diffusive of the acceptable symmetric two-variable limiters, respectively. In our experience, the minmod limiter is more accurate for shock capturing, although the shocks tend to be smeared over many grid points. The minmod gives unacceptable results for the convection problem due to significant diffusion errors which grow over time. The superbee limiter is more accurate for convection problems, but overshoots and undershoots are present at discontinuities in both the shock tube and square wave convection problems. The monotonized central limiter provides a compromise and generally produced the most accurate results.

For the relativistic problems, we compare some of our results with those found in the literature, but caution that such comparisons should be used carefully. There are several possible variations for calculating errors between simulation results and actual values and great detail is generally not included in each literature source. The FDV and TVD errors in this publication were calculated in identical ways. The same can not be confirmed for our comparisons with errors from other publications.

The FDV parameters are noticeably different for the shock problems. The FDV defined variables are smaller than those for the advection problems leading to a more explicit solution method.

4.3.1. Non-relativistic square wave

In this test problem, a square wave is defined with an initial velocity and location. As time increases ($t > 0$), the wave travels and the square profile is maintained. Fig. 5 shows the FDV solution for a square wave that was initially at the left side of the domain. The time step is defined as $\Delta t = \frac{0.8\Delta x}{V_{max}}$ and the FDV defined variables are $\alpha = 0.25$ and $\eta = 0.01$. The results shown in Fig. 5 are at time=0.006 s and are plotted over the exact solution. The initial conditions were given in Table 1. The L1 Norm and L2 Norm errors are shown for the 400 node case in Table 2. This table also shows the errors for the three TVD methods. The convergence of the error values with relation to the size of the spacial steps (100–1600 nodes) are also shown in Fig. 5.

4.3.2. Non-relativistic noh shock

The Noh shock problem was defined by Noh [25]. This problem simulates the shocks produced when two cold (ideal) gasses, initially with high velocity, collide. Two shock waves are created in the collision moving in opposite directions. The inflowing gas between the shocks is heated and comes to rest while the shocks continue to propagate. This test is used to evaluate numerical methods for high speed flow and shock formation. The initial conditions for the problem are given in Table 1. The initial velocity values are equal but in opposite directions around the midpoint (i.e. moving towards each other such that they collide and reflect at $t > 0$). The simulation is symmetric about the center, and the results for the right side 400 node case are shown in Fig. 6. The FDV defined variables for this case are $\alpha = 0.25$ and $\eta = 0.01$. The time step is $\Delta t = \frac{0.25\Delta x}{V_{max}}$. Fig. 6 also shows the FDV errors as compared with the TVD errors (100–1600 nodes). Details of this information for the 400 node case are also give in Table 3.

4.3.3. Non-relativistic shock tube

The shock tube is a common test problem for shock capturing methods. The shock tube is a one-dimensional time dependent problem which initially has two static regions separated by a removable membrane. The initial pressure of the fluid on one side is much higher than that of the fluid on the other. When the membrane is removed, the high pressure fluid quickly expands into the region containing the low pressure fluid. If the initial pressure difference is great enough, a shock front forms. The problem now has five regions. The fluid at each end of the shock tube is undisturbed and has the initial fluid parameters. In the center, there is a rarefaction region, contact discontinuity and shock wave. These states are shown in

Table 1
Initial conditions of the test problems used to verify the FDV method. Note that SI units are used for the non-relativistic cases and natural speed of light units are used for the relativistic cases.

Test problem	Velocity (left)	Velocity (right)	Density (left)	Density (right)	Pressure (left)	Pressure (right)
Square wave	100	100 (wave)	0.05	0.2 (wave)	1.5E3	1.5E3 (wave)
Non-rel shock tube						
Mild	0	0	1.0	0.125	1.0	0.1
Moderate	0	0	1.0	0.02	1.0	1.0E−2
Noh shock	10,000	−10,000	1.0	1.0	7.63E−6	7.63E−6
Rel shock tube						
Lorentz = 1.4	0	0	10.0	1.0	13.3	6.67E−7
Rel Noh shock						
Lorentz = 2.3	0.9c	−0.9c	1.0	1.0	7.63E−6	7.63E−6
Lorentz = 22.4	0.999c	−0.999c	1.0	1.0	7.63E−6	7.63E−6
Lorentz = 224	0.99999c	−0.99999c	1.0	1.0	7.63E−6	7.63E−6
Lorentz = 2236	0.9999999c	−0.9999999c	1.0	1.0	7.63E−6	7.63E−6

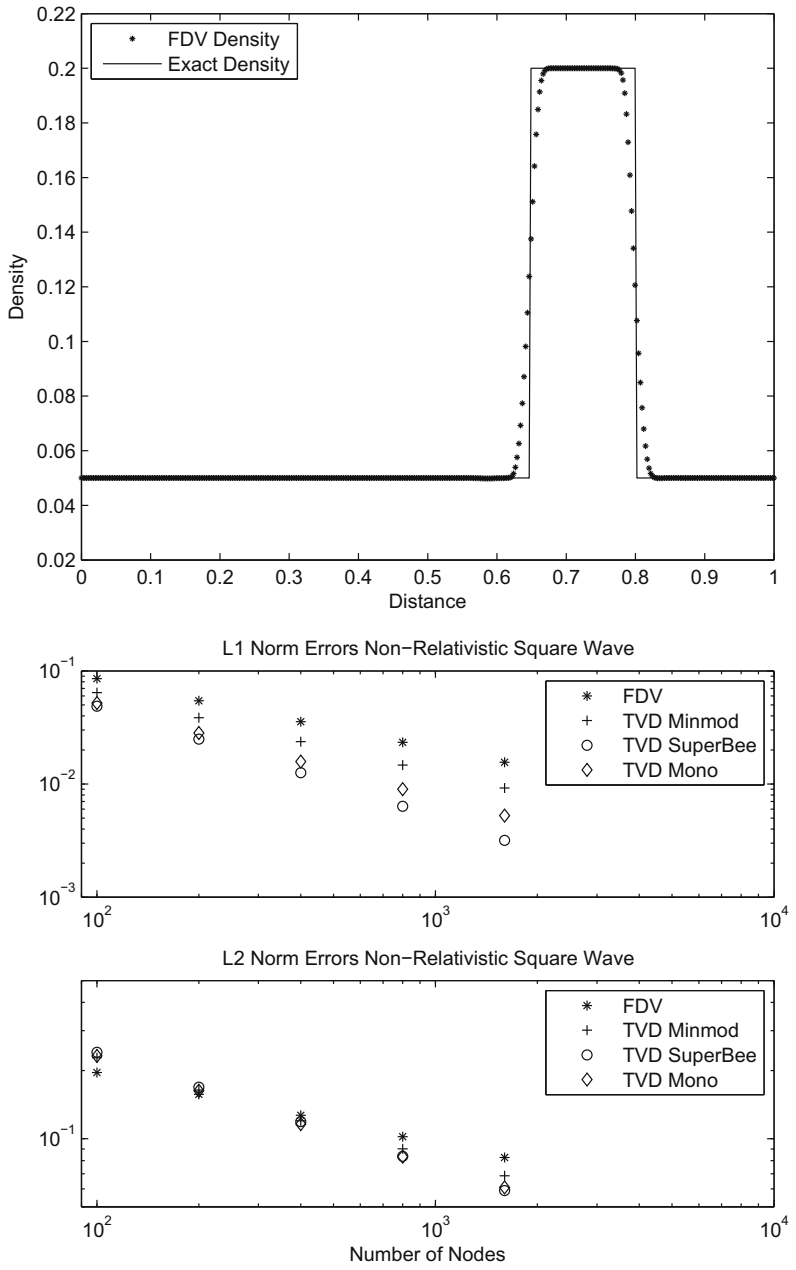

Fig. 5. *Upper Plot:* Non-relativistic square wave with the initial conditions found in Table 1, 400 nodes, specific heat ratio of 5/3 and a time step of $\Delta t = \frac{0.8\Delta x}{V_{max}}$. The FDV defined variables are $\alpha = 0.25$ and $\eta = 0.01$. The square wave was initially started on the left side of the computational domain. This result is for $t = 0.006$ s. *Lower Plot:* The FDV convergence rate for the L1 Norm and L2 Norm density errors of the square wave shown against the TVD errors using domain grids from 100 to 1600 nodes. The L1 Norm and L2 Norm linear best-fit slopes are −0.61 and −0.31.

Table 2
Square wave errors on density with 400 nodes.

Method	E_{L1}	E_{L2}	$E_{L\infty}$
FDV	3.56E−02	1.27E−01	1.48E+00
TVD monotonized central	1.58E−02	1.16E−01	1.87E+00
TVD Minmod	2.37E−02	1.20E−01	1.77E+00
TVD Superbee	1.26E−02	1.19E−01	2.06E+00

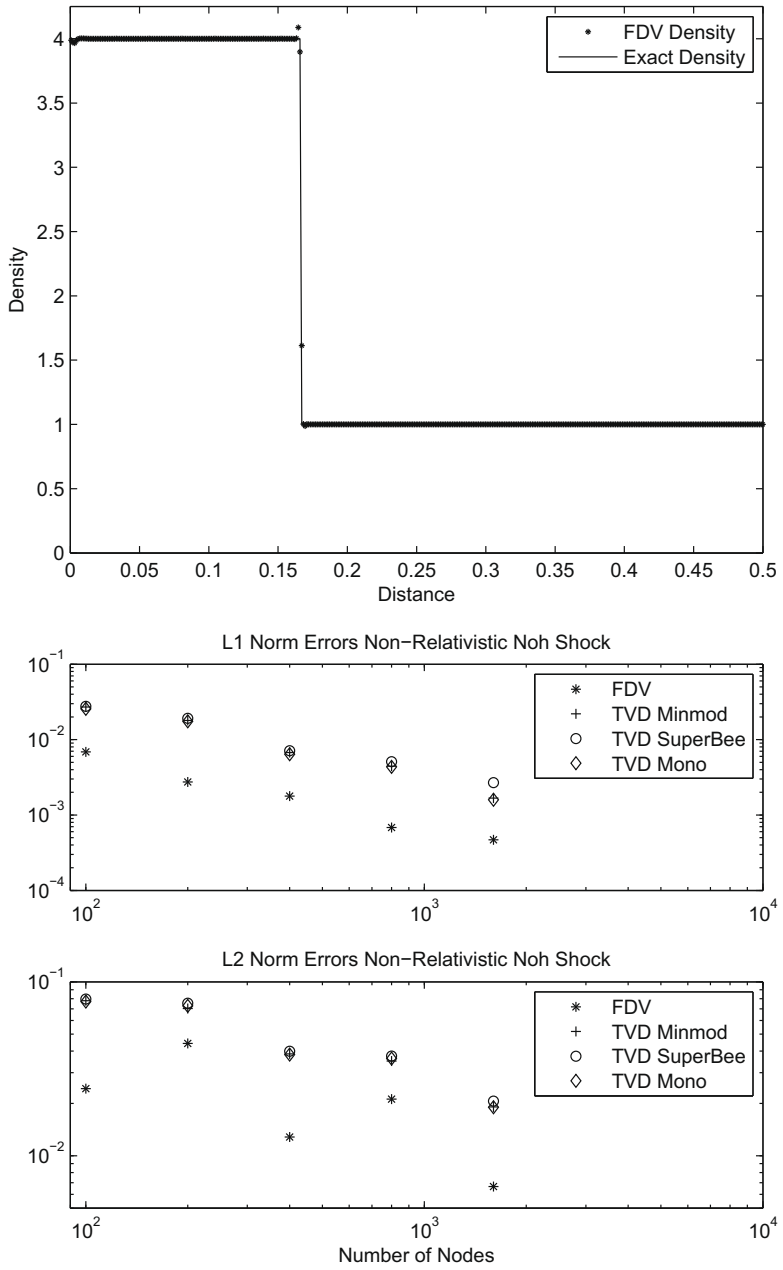

Fig. 6. *Upper Plot:* Right half of the non-relativistic Noh shock with the initial conditions found in Table 1, with 400 nodes and a specific heat ratio of 5/3 and a time step of $\Delta t = \frac{0.25\Delta x}{V_{max}}$. The FDV defined variables are $\alpha = 0.25$ and $\eta = 0.01$. Initially two ideal gasses are flowing towards each other and interact at $x = 0$ resulting in two shocks traveling away from the center. The shock in the figure is traveling to the right and is shown at $t = 5E^{-}5$ s. *Lower Plot:* The FDV convergence rate for the L1 Norm and L2 Norm density errors for the Noh shock shown with the TVD errors using domain grids from 100 to 1600 nodes. The L1 Norm and L2 Norm linear best-fit slopes are −0.97 and −0.48.

Table 3
Non-relativistic Noh shock errors on density with 400 nodes.

Method	E_{L1}	E_{L2}	$E_{L\infty}$
FDV	1.79E−03	1.28E−02	6.13E−01
TVD monotonized central	6.39E−03	3.82E−02	1.80E+00
TVD Minmod	6.74E−03	3.85E−02	1.79E+00
TVD Superbee	7.13E−03	3.99E−02	1.82E+00

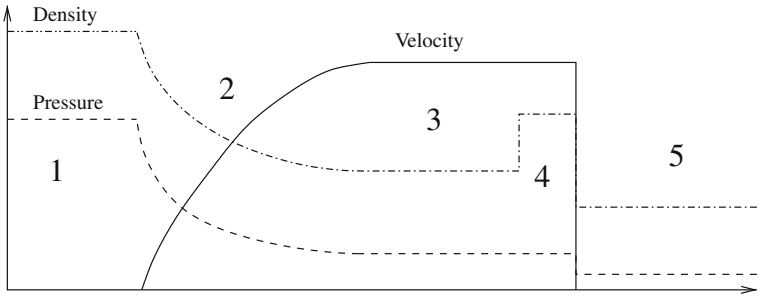

Fig. 7. Transient state of the shock tube. 1, 5: Undisturbed regions with the initial fluid parameters. 2: Rarefaction wave. 3: Contact discontinuity (to the right of the number in the figure). 4: Shock wave (to the right of the number in the figure).

Fig. 7. Region 4, the area between the shock wave and the contact discontinuity, has a different profile depending on the input parameters. For our non-relativistic shocks, this region has a lower magnitude than the relativistic shocks.

Two non-relativistic shock tube cases were run using FDV. The initial conditions for both are given in Table 1. The first shock tube is shown in Fig. 8 at time = 0.15 s. In this figure, density, velocity and pressure are all shown plotted with their respected exact solutions. The FDV parameters are calculated using $\alpha = 0.25$ and $\eta = 0.01$. The highest error in the fit shown by the analytic solution is in the density region behind the shock. The errors for this solution are shown in Table 4.

The second and more difficult non-relativistic shock tube problem solved with FDV is the moderate shock tube using boundary conditions given in Table 1. Fig. 9 shows the results of this case. The figure shows the density, velocity and pressure at time = 0.15 s. The same timestep is used in this case, $\Delta t = \frac{0.25\Delta x}{V_{max}}$ as the lower Mach number case. The errors for this problem are shown in Table 5 and the FDV convergence rate in Fig. 9. In both shock tube cases, the FDV method accurately captures the shock tube profile.

4.3.4. Relativistic shock tube

The special relativistic shock tube is an ideal evaluation technique for mildly ($velocity < 0.9c$) relativistic shocks since there are known solutions allowing the computational method to be tested [7,40]. Additionally, these simulations test the ability of a numerical technique over domains with widely varying flow velocities responsible for large spacial and temporal scale differences. For the mildly relativistic shock, the initial conditions are given in natural units (where $c = G = 1$) in Table 1 [7,17]. The tube is one unit in length with the initial contact discontinuity located in the center. In the mildly relativistic shock case, 400 nodes are used with a time step of $\Delta t = \frac{0.2\Delta x}{V_{max}}$.

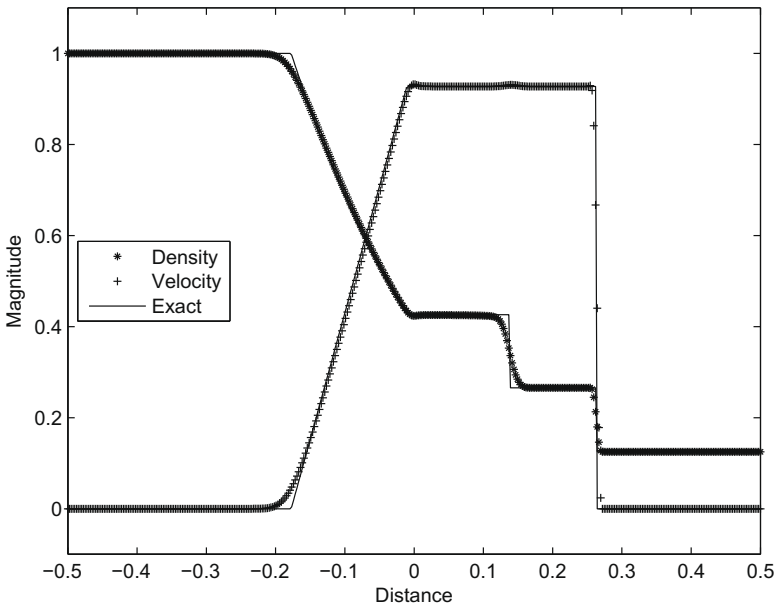

Fig. 8. Non-relativistic shock tube with the parameters found in Table 1 with 400 nodes, specific heat ratio of 1.4 and a time step of $\Delta t = \frac{0.25\Delta x}{V_{max}}$. The FDV defined variables are $\alpha = 0.25$ and $\eta = 0.01$. The time shown is 0.15 s.

Table 4
Non-relativistic mild shock tube density errors, for the 400 node case.

Method	E_{L1}	E_{L2}	$E_{L\infty}$
FDV	5.71E−03	1.14E−02	2.85E−01
TVD monotonized central	2.95E−03	1.19E−02	2.97E−01
TVD Minmod	4.14E−03	1.27E−02	2.66E−01
TVD Superbee	3.43E−03	1.22E−02	3.08E−01

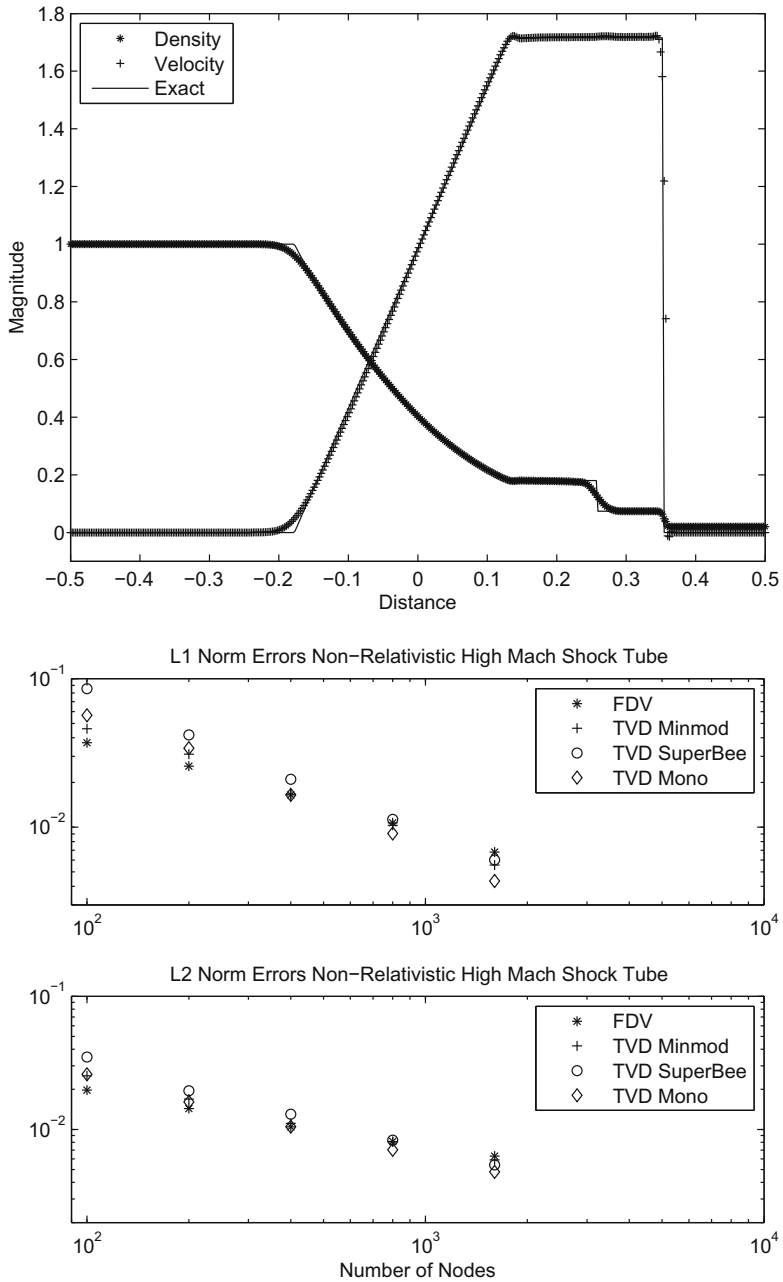

Fig. 9. *Upper Plot:* Moderate shock tube with the parameters found in Table 1 with 400 nodes, specific heat ratio of 1.4 and a time step of $\Delta t = \frac{0.25\Delta x}{V_{max}}$. The FDV defined variables are $\alpha = 0.25$ and $\eta = 0.01$. The time shown is 0.15 s. *Lower Plot:* Convergence rate of L1 Norm and L2 Norm density errors for the moderate shock tube using domain grids from 100 to 1600 nodes. The L1 Norm and L2 Norm linear best-fit slopes are −0.62 and −0.41.

Table 5
Non-relativistic moderate shock tube density errors for the 400 node case.

Method	E_{L1}	E_{L2}	$E_{L\infty}$
FDV	1.65E−02	1.05E−02	1.34+E00
TVD monotonized central	1.65E−02	1.05E−02	7.69E−01
TVD Minmod	1.67E−02	1.11E−02	1.32E+00
TVD Superbee	2.10E−02	1.30E−02	1.08E+00

Fig. 10 shows the results of the mildly relativistic (Lorentz factor = 1.4) shock tube simulation. The figure contains the velocity in speed of light coordinates, the normalized pressure and the normalized density. The analytic solution is plotted beneath the FDV solution as shown by the solid line. We see a decrease in the sharpness of the fit around the shock as the Lorentz factor increases.

4.3.5. Ultra-relativistic noh shock simulation

In order to test our technique in the ultra-relativistic regime, we conducted a series of planar shock reflection simulations for which the analytic solution was found by Blandford and McKee [6]. This problem is similar to the non-relativistic Noh shock problem. The initial conditions for these simulations (in natural units) are given in Table 1. Fig. 11 shows the profiles for the resulting solution found from an initial velocity of 0.9c (Lorentz factor = 2.3). The simulation was run with 400 spacial nodes (only the right half of the simulation is shown in Fig. 11) and a time step of $\Delta t = \frac{0.5\Delta x}{V_{max}}$.

Fig. 12 shows the physical profiles when various initial velocities (Lorentz factor = 2.3–2236) were used. For the purpose of comparison, all the solutions are shown using the same time step. Visually, the shock is well captured with a small amount of dispersion at the discontinuity. Considering the change in scale for the densities, the FDV method continues to accurately capture the discontinuity as the Lorentz factor increases.

The L-1 Norm errors for the velocity = 0.9c (Lorentz factor = 2.3) simulation are shown in Table 6 along with a comparison with other methods. This table includes results found by Anninos and Fragile [2] using a non-oscillatory central difference (NOCD) scheme and [1] using an approximate Riemann solver. We find that the FDV method is more accurate at the boundary $x = 0$, where many numerical methods tend to be disrupted, but slightly more diffuse at the shock than the solutions found with the above references. Fig. 11 shows the FDV convergence rate for this problem. Our results are very comparable with those of other numerical methods for these ultra-relativistic simulations.

4.4. Converging/diverging nozzle

The converging/diverging nozzle was developed in the late 1800s by Gustaf de Laval and has become a classical analytic fluids problem demonstrating subsonic and supersonic flow [21]. Fig. 13 shows the physical characteristics of the nozzle. The

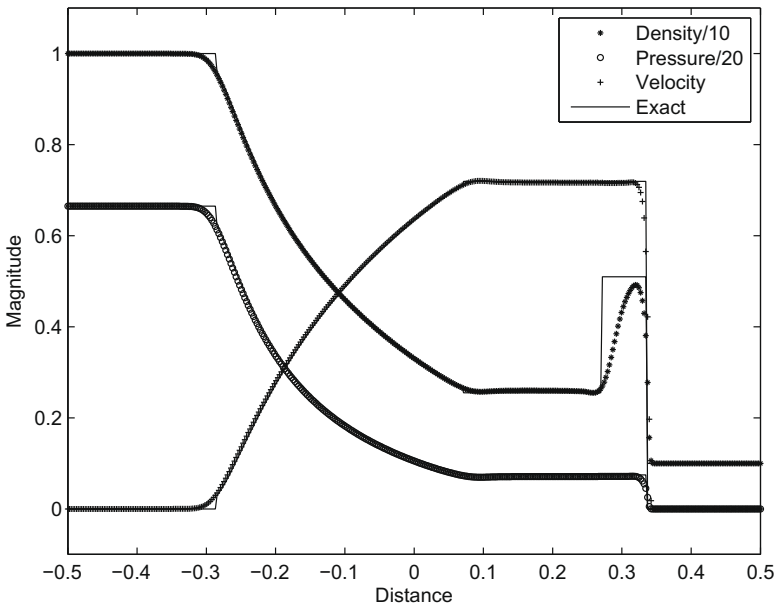

Fig. 10. FDV solution of a mildly relativistic (Lorentz factor = 1.4) shock tube with the initial conditions given in Table 1. The analytic solution is plotted over the computational solution. Density and pressure are normalized for comparison with velocity. This simulation was run with 400 nodes, a time step of $\Delta t = \frac{0.2\Delta x}{V_{max}}$ and is displayed at $t = 0.3$ (natural speed of light units). The specific heat ratio is 5/3. The FDV defined variables are $\alpha = 0.25$ and $\eta = 0.01$.

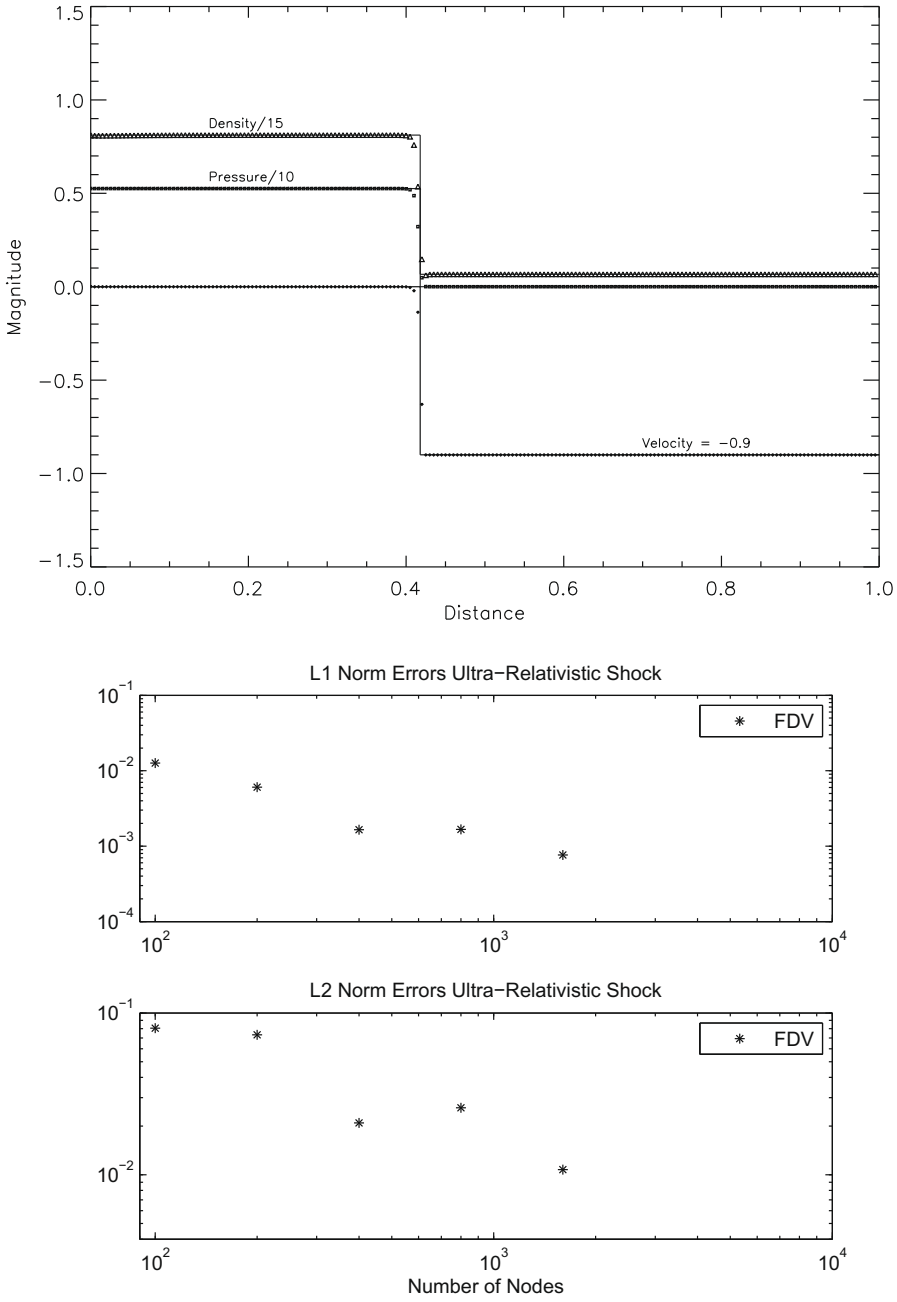

Fig. 11. *Upper Plot:* Demonstration of strong shock capturing using the FDV method. The physical planar shock solution as described in the text is shown at $t = 2.0$ (natural speed of light units). Initial opposing velocities of 0.9c (Lorentz factor = 2.3) were applied, and 200 spacial nodes (the right half) are shown. Density and pressure are normalized by the shown factor for comparison with velocity. The time step used was $\Delta t = \frac{0.5\Delta x}{V_{max}}$ and the specific heat ratio is 4/3. The FDV defined variables are $\alpha = 0.25$ and $\eta = 0.01$. The analytic solution is shown with solid lines. *Lower Plot:* FDV convergence rate for the L1 Norm and L2 Norm density errors for the highly relativistic shock using domain grids from 100 to 1600 nodes. The L1 Norm and L2 Norm linear best-fit slopes are -0.996 and -0.73.

initial area decreases along the nozzle (converges) to a point of minimum area at the throat. The area then increases (diverges) to the exit. The inlet flow parameters are set on the left side of the nozzle. The flow through the nozzle is determined by the back pressure that is controlled outside of the exit. As the back pressure is decreased, the flow velocity through the nozzle increases. The converging region will always be subsonic as the flow chokes at the throat with a Mach number of 1. The pressure in the throat will always be less than the inlet pressure. The flow in the diverging region can reach supersonic speeds. If the diverging region is subsonic it acts as a diffuser and the pressure increases between the throat and exit. If the

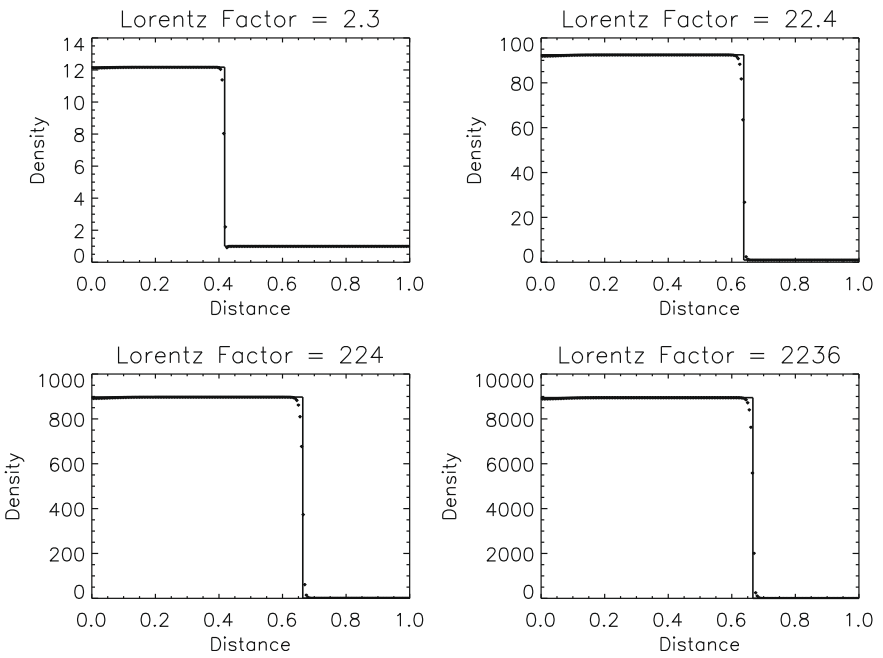

Fig. 12. Resulting density from the ultra-relativistic (Lorentz factor = 2.3–2236) planar shock reflection simulation using the FDV method. Initially opposing fluid velocities of the four magnitudes shown were applied with 200 spacial nodes (the right half) shown. The displayed time for these simulations is 2.0 (natural speed of light units) and the time step used was $\Delta t = \frac{0.5\Delta x}{V_{max}}$. The FDV defined variables are $\alpha = 0.25$ and $\eta = 0.01$. The analytic solution is shown with solid lines.

Table 6
L-1 Norm errors in the primitive variables for the planar wall shock simulation with 400 nodes and velocity = 0.9*c*.

Method	Velocity	Density	Pressure
FDV	1.50E−03	1.65E−03	2.11E−03
NOCD[a]	2.69E−03	3.26E−02	1.10E−02
AR[b]	8.03E−03	9.66E−03	9.07E−03

[a] Anninos and Fragile [2].
[b] Aloy et al. [1].

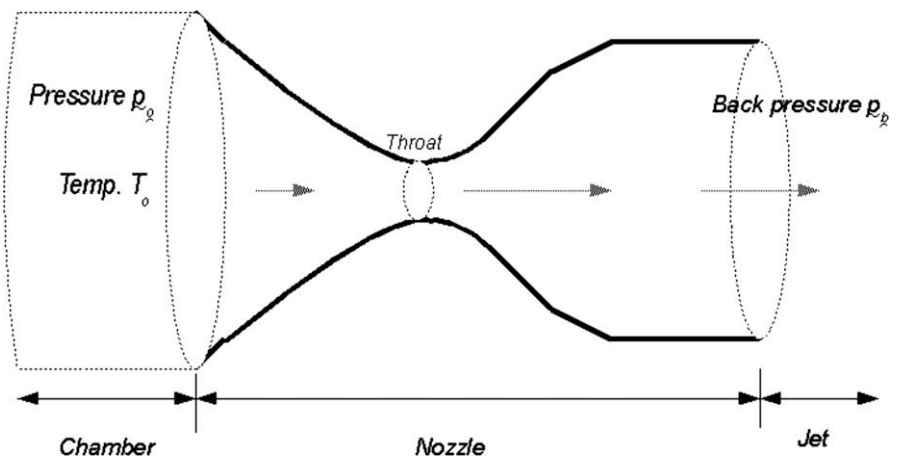

Fig. 13. Converging/Diverging (de Laval) nozzle. The minimum area is the throat of the nozzle. Given initial flow conditions at the nozzle inlet, the flow properties through the nozzle are determined by the exit pressure (or back pressure).

diverging region is supersonic it acts as a nozzle and the pressure decreases between the throat and exit. The back pressure determines the type of flow in the diverging region. If the back pressure is sufficiently low at the exit, a normal shock will

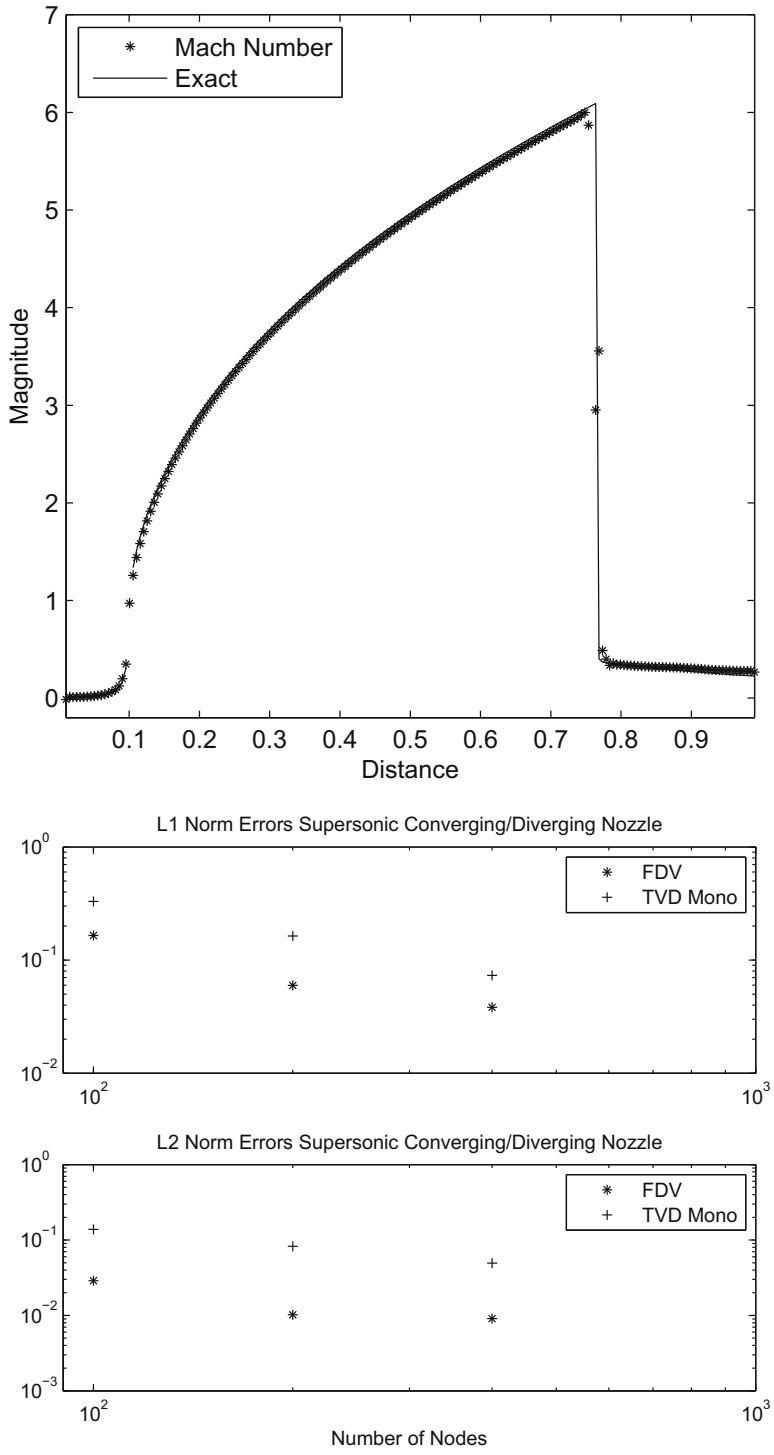

Fig. 14. *Upper Plot:* Mach number results from the converging/diverging nozzle test after steady state has been reached ($t = 0.014$ s) with 200 nodes. The back pressure is $0.004P_0$ and the nozzle chokes at the neck with a Mach number of 1. The time step used was $\Delta t = \frac{0.5\Delta x}{V_{max}}$ and the specific heat ratio is 4/3. The FDV defined variables are $\alpha = 0.6$ and $\eta = 0.1$. The analytic solution is shown with solid line, but has a break at the throat since an analytic solution is not possible at that location. *Lower Plot:* FDV convergence rate for the L1 Norm and L2 Norm velocity errors. The L1 Norm and L2 Norm linear best-fit slopes are -1.05 and -0.83.

Table 7
de Laval density errors for the 400 node case.

Method	E_{L1}	E_{L2}	$E_{L\infty}$
FDV	3.83E−02	3.83E−03	8.51E−01
TVD monotonized central	7.32E−02	4.94E−02	8.05E−01

develop in the region between the nozzle throat and exit plane. In such a situation the flow accelerates subsonically from the inlet to the throat, transitions smoothly to supersonic flow, expands supersonically to some point downstream, then transitions abruptly to subsonic flow across the shock wave and decelerates subsonically to the exit. This is an interesting numerical problem since there are regions of both incompressible and compressible flow.

The isentropic converging/diverging nozzle was solved numerically with FDV using the hydrodynamic equations from Eq. (10) and compared with the known properties of the flow. The following relations are known where the inlet (or stagnation) properties for area, pressure and density are given by A_0, P_0 and ρ_0 and all are a function of distance including the Mach number.

$$\frac{A}{A_{throat}} = \frac{1}{M}\left[\left(\frac{2}{\gamma+1}\right)\left(1+\frac{\gamma-1}{2}M^2\right)\right]^{\frac{\gamma+1}{2(\gamma-1)}}, \tag{43}$$

$$\frac{P_0}{P} = \left[1+\frac{\gamma-1}{2}M^2\right]^{\frac{\gamma}{\gamma-1}}, \tag{44}$$

$$\frac{\rho_0}{\rho} = \left[1+\frac{\gamma-1}{2}M^2\right]^{\frac{1}{\gamma-1}}. \tag{45}$$

Eq. (43) results in two solutions for the Mach number at each position along the nozzle corresponding to the subsonic and supersonic values. For a subsonic solution with a shock, the shock can be resolved using the following jump conditions where "1" is the shocked region and "2" is the unshocked region.

$$M_2^2 = \frac{M_1^2+\frac{2}{\gamma-1}}{\frac{2\gamma}{\gamma-1}M_1^2-1}, \tag{46}$$

$$P_2 = P_1\left(\frac{1+\gamma M_1^2}{1+\gamma M_2^2}\right), \tag{47}$$

$$\rho_2 = \rho_1\left(\frac{M_1^2 P_1}{M_2^2 P_2}\right). \tag{48}$$

For the test problem presented, the nozzle geometry is give by;

$$r(x) = \begin{cases} -2x+0.25 & x \leqslant 0.1 \\ 0.5x & x > 0.1 \end{cases} \tag{49}$$

The initial conditions at the inlet are given as; Pressure = 10 bar, density = 17.7 kg/m^3 and velocity = 0 m/s. The exit pressure was held constant for a variety of test runs starting at 10 bar and then lowered. The results presented have a back pressure or $0.004P_0$ which is low enough for supersonic flow in the diverging region and for a shock to form. The FDV defined variables are $\alpha = 0.6$ and $\eta = 0.1$. The simulation was allowed to run until steady state conditions were met. The other exit boundary conditions are calculated from the known solution given in the above equations.

Results from the FDV simulations are shown in Fig. 14. This 200 node simulation captured all the flow details in this example problem including the pre-throat converging subsonic region, the post-throat diverging supersonic region and the shock. This flow includes both incompressible and compressible regions as seen in the Mach number plot given in Fig. 14. The TVD Monotonized Central scheme was also used for this simulation and the error results are given along with the TVD results in the figure. A comparison of the errors is shown in Table 7 for the 400 node case comparing the FDV and TVD methods.

5. Summary

We have presented a variety of test problems to demonstrate the capabilities of the finite element formulation of the Flowfield Dependent Variation method. These problems included smooth flows, shocks, incompressible, compressible, subsonic, supersonic and relativistic flows. The converging/diverging nozzle simulation was presented to demonstrate a solution with both compressible and incompressible flow in the domain. These simulations show the ability of FDV to solve flowfields with highly varying flow velocities indicating large variations in spatial and temporal scales. The ability to solve such flowfields is crucial for the numerical study of the complex interactions. Our errors across the flowfield are comparable with those of finite difference methods which have been studied much more extensively in the literature.

There are three primary motivators in our simulation domain for choosing a finite element formulation. First, finite element schemes allow for unstructured grids while finite difference schemes do not (some finite volume schemes do allow unstructured grids). Our goal to develop an MHD solver means that the complex geometry of reconnecting field lines will benefit from an unstructured grid. Second, flux boundary conditions can be exactly applied without the use of phantom nodes or other approximations. This is important at the edge of a domain where energy and density flux is prevalent. Third, curvilinear coordinate systems can be implemented without dead zones due to the forward/backward nature of finite difference schemes. All the elements (node regions) are simultaneously solved in finite element schemes. In finite difference schemes each node is solved in relation to the nodes surrounding it. This can create small flow field voids in curvilinear coordinates. The major disadvantage for traditional finite element schemes is the computations due to large matrix inversion calculations. In recent years, studies have provided alternatives for these large inversions. The calculations presented in this paper have utilized the element-by-element formulation to decrease the size of the matrix inversions [31]. For the one-dimensional calculations, the results were also found using a straight forward single large matrix inversion to ensure consistent results. All of these motivators lead us to choose a finite element method.

The advantages of the FDV method include the following; First, physical flow properties dictate the solution type which allows Different flow regions (in the same simulation) to have different solution formulations. Second, a wide range of flow types (for example incompressible and compressible) can be solved in a single simulation. Third, the use of Jacobians contribute to integration stability. The strengths of the finite element FDV method are necessary for the applications of interest, magnetic reconnection in both stellar scale and laboratory scale plasmas. The FDV method has the potential to handle the vast scale differences between the two problems while also maintaining an accurate solution for the complex physics.

Acknowledgments

This work was supported by the UA Huntsville University Research Infrastructure Investment Grant and also by NSF Grant ATM-0754378 and AFOSR Grant FA9550-07-1-0468 at the UA Huntsville Center for Space Plasma and Aeronomic Research.

References

[1] M.A. Aloy, J.M. Ibáñez, J.M. Martí, GENESIS: a high-resolution code for three-dimensional relativistic hydrodynamics, ApJS 122 (1999) 151.
[2] P. Anninos, P.C. Fragile, Nonoscillatory central difference and artificial viscosity schemes for relativistic hydrodynamics, ApJS 144 (2003) 243.
[3] P. Arminjon, R. Touma, Central finite volume methods with constrained transport divergence treatment for ideal MHD, J. Comput. Phys. 204 (2005) 737.
[4] D.S. Balsara, Total variation diminishing scheme for relativistic magneto-hydrodynamics, ApJS 132 (2001) 83.
[5] D.S. Balsara, Second-order accurate schemes for magnetohydrodynamics with divergence-free reconstruction, ApJS 151 (2004) 149.
[6] R.D. Blandford, C.F. McKee, Fluid dynamics of relativistic blast waves, Phys. Fluids 19 (1976) 1130.
[7] J. Centrilla, J.R. Wilson, Planar numerical cosmology II. The difference equations and numerical tests, ApJS 54 (1984) 229.
[8] T.J. Chung, Transitions and interactions of inviscid/viscous, compressible/incompressible and laminar/turbulent flows, Int. J. Numer. Meth. Fluids 31 (1999) 223.
[9] T.J. Chung, Computational Fluid Dynamics, Cambridge University Press, New York, 2002.
[10] B. Cockburn, C.W. Shu, The Runge–Kutta discontinuous Galerkin method for conservation laws V: multidimensional systems, J. Comput. Phys. 141 (1999) 199.
[11] R. Courant, K. Friedrichs, H. Lewy, On the partial difference equations of mathematical physics, IBM J. (1967) 215 (English translation of the 1928 German original).
[12] L. Del Zanna, N. Bucciantini, P. Londrillo, An efficient shock-capturing central-type scheme for multidimensional relativistic flows II. Magnetohydrodynamics, A&A 400 (2003) 397.
[13] M. Dumbser, D.S. Balsara, E.F. Toro, C.D. Munz, A unified framework for the construction of one-step finite-volume and discontinuous Galerkin schemes, J. Comput. Phys. 227 (2008) 8209.
[14] J.A. Font, Numerical hydrodynamics and magnetohydrodynamics in general relativity, 2008, Liv. Rev. in Rel., lrr-2008-7.
[15] S. Fromang, P. Hennebelle, R. Teyssier, A high order Godunov scheme with constrained transport and adaptive mesh refinement for astrophysical magnetohydrodynamics, Astron. Astrophys. 457 (2006) 371.
[16] A. Glasser, C. Sovinec, R. Nebel, T. Gianakon, S. Plimpton, M. Chu, et al, The NIMROD code: a new approach to numerical plasma physics, Plasma Phys. Controll. Fusion 41 (1999) 47.
[17] J.F. Hawley, L.L. Smarr, J.R. Wilson, A numerical study of nonspherical black hole accretion I. Equations and test problems, ApJ 277 (1984) 296.
[18] C. Hu, C.W. Shu, Weighted essentially non-oscillatory schemes on triangular meshes, J. Comput. Phys. 150 (1999) 97.
[19] G.S. Jiang, C. Shu, Efficient implementation of weighted ENO schemes, J. Comput. Phys. 126 (1996) 202.
[20] C.T. Kelley, Iterative Methods for Linear and Nonlinear Equations, SIAM, Philadelphia, 1995.
[21] L.D. Landau, E.M. Lifshitz, Fluid Mechanics Course of Theoretical Physics, vol. 6, Butterworth-Heinemann Oxford, 1987.
[22] B. Leer, Towards the ultimate conservative difference scheme. IV. A new approach to numerical convection, J Comput. Phys. 23 (1977) 276.
[23] J.M. Martí, E. Muller, Numerical hydrodynamics in special relativity, 2003, Liv. Rev. in Rel., lrr-2003-7.
[24] D.L. Meier, Multidimensional astrophysical structural and dynamical analysis I. Development of a nonlinear finite element approach, ApJ 518 (1999) 788.
[25] W.F. Noh, Errors for calculations of strong shocks using an artificial viscosity and an artificial heat flux, J. Comput. Fluids 72 (1987) 78.
[26] R. Peterkin, M. Frese, C. Sovinec, Transport of magnetic flux in an arbitrary coordinate ALE code, J. Comput. Phys. 140 (1998) 148.
[27] S. Qamar, G. Warnecke, a high order kinetic flux-spitting method for the special relativistic magnetohydrodynamics, J. Comput. Phys. 205 (2005) 182.
[28] G.A. Richardson, The development and application of the finite element general relativistic flow and shock solver, Ph.D. Thesis, University of Alabama in Huntsville, 2000.
[29] G.A. Richardson, T.J. Chung, Computational relativistic astrophysics using the flow field-dependent variation method, ApJS 139 (2002) 539.
[30] Y. Saad, M. Schultz, GMRES: a generalized minimal residual algorithm for solving nonsymmetric linear systems, SIAM J. Sci. Stat. Comput. 7 (1996) 856.
[31] Y. Saad, Iterative Methods for Sparse Linear Systems, PWS Publishing, Boston, 1996.
[32] K. Sankaran, L. Martinelli, S. Jardin, E. Choueiri, A flux-limited numerical method for solving the MHD equations to simulate propulsive plasma flows, Int. J. Numer. Meth. Eng. 53 (2002) 1415.

[33] G. Schunk, F. Canabal, G. Heard, T.J. Chung, Unified CFD methods via flowfield-dependent variation theory, AIAA (1999) 99–3715.
[34] B.A. Schutz, First Course in General Relativity, Cambridge University Press, 1985.
[35] G.A. Sod, A survey of several finite difference methods for systems of nonlinear hyperbolic conservation laws, J. Comput. Phys. (1978) 27 1.
[36] C. Sovinec, T. Gianakon, E. Held, S. Kruger, D. Schnack, et al, NIMROD: a computational laboratory for studying nonlinear fusion magnetohydrodynamics, Phys. Plasmas 10 (2003) 1727.
[37] C. Sovinec, A. Glasser, T. Gianakon, D. Barnes, R. Nebel, S. Kruger, D. Schnack, S. Plimpton, A. Tarditi, M. Chu, Nonlinear magnetohydrodynamics with high-order finite elements, J. Comput. Phys. 195 (2004) 355.
[38] H. Tang, K. Xu, A high-order gas-kinetic method for multidimensional ideal magnetohydrodynamics, J. Comput. Phys. 165 (2000) 69.
[39] R. Teyssier, S. Fromang, E. Dormy, Kinematic dynamos using constrained transport with high order Godunov schemes and adaptive mesh refinement, J. Comput. Phys. 218 (2006) 44.
[40] K.W. Thompson, The special relativistic shock tube, J. Fluid Mech. 171 (1986) 365.
[41] G. Tóth, D. Odstril, Comparison of some flux corrected transport and total variation diminishing numerical schemes for hydrodynamic and magnetohydrodynamic problems, J. Comput. Phys. 128 (1996) 82.
[42] H.C. Yee, A class of high-resolution explicit and implicit shock-capturing methods, NASA TM-101088, 1989.
[43] K.T. Yoon, S.Y. Moon, S.A. Garcia, G.W. Heard, T.J. Chung, Flowfield-dependent mixed explicit–implicit (FDMEI) methods for high and low speed and compressible and incompressible flows, Comput. Meth. Appl. Mech. Eng. 151 (1998) 75.
[44] O.C. Zienkiewicz, The Finite Element Method, 3rd ed., McGraw-Hill, U.K., 1977.